Check for updates

NANO · MICRO small
www.small-journal.com

Nickel Oxide Hole Injection Layers for Balanced Charge Injection in Quantum Dot Light-Emitting Diodes

*Haoyue Wan, Eui Dae Jung, Tong Zhu, So Min Park, Joao M. Pina, Pan Xia, Koen Bertens, Ya-Kun Wang, Ozan Atan, Haijie Chen, Yi Hou, Seungjin Lee, Yu-Ho Won, Kwang-Hee Kim, Sjoerd Hoogland, and Edward H. Sargent**

Quantum dot (QD) light-emitting diodes (QLEDs) are promising for next-generation displays, but suffer from carrier imbalance arising from lower hole injection compared to electron injection. A defect engineering strategy is reported to tackle transport limitations in nickel oxide-based inorganic hole-injection layers (HILs) and find that hole injection is able to enhance in high-performance InP QLEDs using the newly designed material. Through optoelectronic simulations, how the electronic properties of NiO_x affect hole injection efficiency into an InP QD layer, finding that efficient hole injection depends on lowering the hole injection barrier and enhancing the acceptor density of NiO_x is explored. Li doping and oxygen enriching are identified as effective strategies to control intrinsic and extrinsic defects in NiO_x, thereby increasing acceptor density, as evidenced by density functional theory calculations and experimental validation. With fine-tuned inorganic HIL, InP QLEDs exhibit a luminance of 45 200 cd m^{-2} and an external quantum efficiency of 19.9%, surpassing previous inorganic HIL-based QLEDs. This study provides a path to designing inorganic materials for more efficient and sustainable lighting and display technologies.

1. Introduction

Quantum dots (QDs) have gained significant attention as a next-generation light-emitting material due to their high color purity, high emission efficiencies, and ease of processing.[1] Photoluminescence quantum efficiencies (PLQE) approaching unity have been demonstrated through the optimization of the chemical composition, design of the core–shell structures, and surface-passivating ligands.[2] InP-based QDs have been successfully employed in liquid crystal displays as color converters.[3] The success of this technology has led to increased interest in directly-emitting QD-based light-emitting diodes (QLEDs) to provide ultrawide color gamut, low energy consumption, flexibility, and low cost for next-generation displays.[4]

Poly(3,4-ethylenedioxythiophene):poly (styrene sulfonate) (PEDOT:PSS) is a popular hole injection layer (HIL) due to its well-positioned highest occupied molecular orbital (HOMO) level; however, its acidic nature degrades the transparent conductive oxide, resulting in diminished device performance.[5] NiO_x has emerged as a potential PEDOT:PSS substitute, delivering an average external quantum efficiency (EQE) of 17.2% compared to 16.1% for PEDOT:PSS in InP QLEDs. Additionally, it enhances device stability, extending the T_{75} lifetime from 40 to 74 h at an initial luminance of 2500 cd m^{-2}.[6] Previous advancements employed self-assembled monolayers (SAMs) on NiO_x to improve charge injection. However, these devices continue to experience imbalanced charge carrier injection, which remains the key limiter preventing high luminance and emission efficiencies in QLEDs.[7] Enhancing charge injection by controlling the properties of NiO_x is a crucial strategy for improving device performance.

In this study, we employed optoelectronic simulations to investigate the role of defects in NiO_x as HIL for efficient hole injection. The simulations revealed that NiO_x HILs engineered to have a lower valence band maximum (VBM) and a higher acceptor density exhibit significantly improved hole injection compared to a control NiO_x layer. Through density functional theory (DFT) calculations and experimental validation, we identified Li doping and oxygen enriching as effective strategies to control intrinsic and extrinsic defects in NiO_x. As a result, we developed a process to dope NiO_x with Li ions and use UV ozone treatments to enrich it with oxygen. The resulting QLED devices exhibited noticeable improvement compared to the control devices with undoped NiO_x. The maximum luminance (L_{Max}) increases from 27 300 to 45200 cd m^{-2}, and the EQE increases from 19.2% to 19.9%, setting a new record EQE achieved for inorganic HIL-based InP QLEDs.

H. Wan, E. D. Jung, T. Zhu, S. M. Park, J. M. Pina, P. Xia, K. Bertens, Y.-K. Wang, O. Atan, H. Chen, Y. Hou, S. Lee, S. Hoogland, E. H. Sargent
Department of Electrical and Computer Engineering
University of Toronto
35 St George Street, Toronto, Ontario M5S 1A4, Canada
E-mail: ted.sargent@utoronto.ca
Y.-H. Won, K.-H. Kim
Samsung Advanced Institute of Technology
Samsung Electronics
Suwon 16678, Republic of Korea

The ORCID identification number(s) for the author(s) of this article can be found under https://doi.org/10.1002/smll.202402371

DOI: 10.1002/smll.202402371

 © 2024 Wiley-VCH GmbH

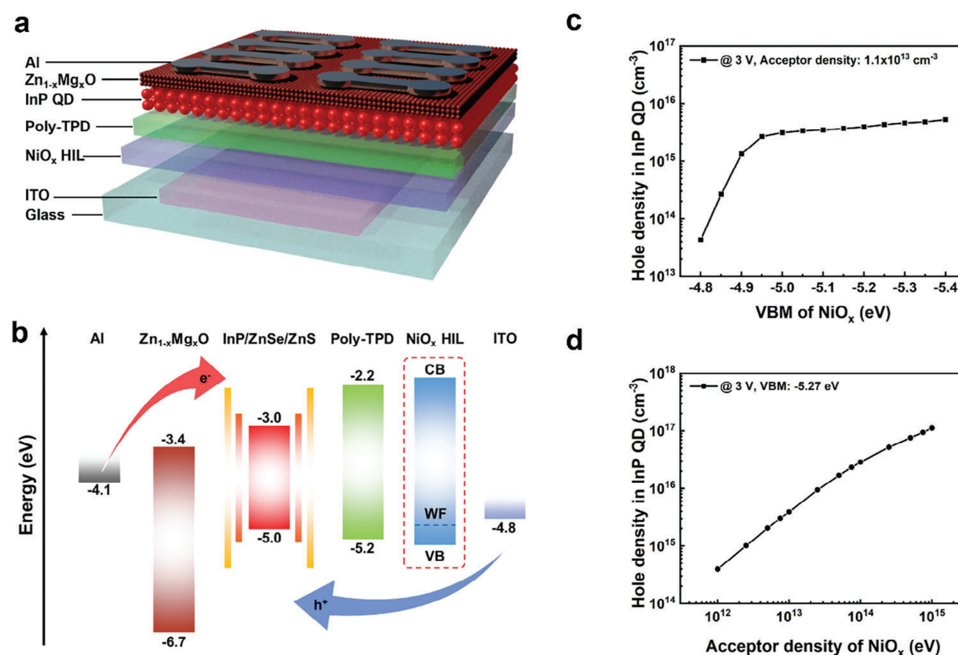

Figure 1. Optoelectronic simulations of InP QLEDs. a) Device structure of InP QLEDs with NiO_x HIL. b) Energy level diagram of InP QLEDs. Simulation results of the hole density at the center of InP QD at 3 V c) with different VBM and d) with different acceptor densities of NiO_x.

2. Result

A widely used QLED device p-i-n architecture was adopted in this work (**Figure 1a**). The band alignment of the HIL material needs to be favorable for hole injection into the QD layer without having to overcome an energy barrier (Figure 1b).[6,8] We utilized optoelectronic simulations based on the Solar Cell Capacitance Simulator (SCAPS) where we varied the electronic properties of NiO_x and monitored the ability to inject holes into the QD layer.[9] We first simulated the hole density in the InP QD layer for different NiO_x VBM values (Figure 1c). The simulations predict that the hole injection increases rapidly with decreasing VBM until a NiO_x VBM of −5.0 eV, where the energetic barrier between the HIL and poly-TPD hole transfer layer (HTL) can be surpassed by thermal processes at room temperature. We then explored the impact of the NiO_x acceptor density on the hole injection into the InP QD layer (Figure 1d) and found that the hole density in the InP QDs increases significantly with increasing acceptor density. Based on these simulation results, we predicted that the performance of QLEDs could be optimized by combining a high NiO_x acceptor density and a VBM level deeper than −5.0 eV.

Experimentally, the VBM of NiO_x can be tuned by using interface treatment and alloying,[10] and the acceptor density in NiO_x can be tuned by the ratio of Ni^{3+}/Ni^{2+} through external doping.[11] To guide intrinsic and extrinsic defect engineering strategies for the control of structural and electronic properties of NiO_x, we used DFT calculations to investigate the defect formation mechanism in NiO_x.

The point defect properties of NiO_x, which include intrinsic defects ($V_O^{0,+1,+2}$, $V_{Ni}^{0,-1,-2}$) and extrinsic defects ($A_{Ni}^{0,-1}$, A = (Li, Na, K, Rb, Cs, Cu, Ag)) were explored through the supercell approach by DFT (Details in the Experimental Section and Note S1, Supporting Information). The composition of NiO_x is described using x and varies between two limits: the Ni-poor/O-rich limit (point A: $\Delta\mu_{Ni} = -3.17$ eV, $\Delta\mu_O = -0.24$ eV) and the Ni-rich/O-poor limit (point B: $\Delta\mu_{Ni} = 0$ eV, $\Delta\mu_O = -3.41$ eV) (**Figure 2a**). Based on these two limit conditions, the defect formation energies in the charge-neutral state were explored (Figure 2b) to show that the extrinsic acceptor-like dopants (Li, Na, K, Cu) can be easily doped into the NiO_x as their formation energies are lower than the intrinsic ones, V_{Ni}.

Next, the study of transition energy levels of point defects, illustrated in Figure 2c, reveals that dopants such as Li, Na, K, and Rb enhance hole densities and correspondingly improve hole conductivity. This improvement is due to these dopants creating acceptor-like defects and shallow traps, in contrast to the deep traps formed by the intrinsic donor-like defect V_O. The impact of defect formation on the Fermi levels, which correlates with the acceptor density, was investigated (Figure 2d,e; Figure S2, Supporting Information) through charge state defect formation energy calculations with DFT.

For the intrinsic case (Figure 2d), we found that the Fermi level can be effectively tuned by adjusting the Ni:O ratio. When the oxygen concentration increases, the hole transport rises (Fermi level pinned by V_O and V_{Ni}, as seen in points B, C, and D) and then falls (Fermi level pinned only by the transition level of V_{Ni} (0/-1), as seen in points E, A) under high oxygen concentrations.

For the extrinsic defects, we calculated four shallow defects with Li, Na, K, and Rb dopants (Figure S2, Supporting Information) and focused on the Li dopant, since its ionic radius (Li^{1+}, 76 pm) is similar to Ni^{2+} (69 pm) and has successfully been incorporated in NiO_x.[12] As shown in Figure 2e, we found similar trends as in the intrinsic case. When the NiO_x changes from O-poor to O-rich conditions, the hole concentration first increases and then drops, since the fermi level is first pinned by the V_O and Li_{Ni}, and then by the transition level of Li_{Ni}(0/-1)). By

© 2024 Wiley-VCH GmbH

16136829, 0, Downloaded from https://onlinelibrary.wiley.com/doi/10.1002/smll.202402371 by University Of Toronto Libraries, Wiley Online Library on [11/04/2024]. See the Terms and Conditions (https://onlinelibrary.wiley.com/terms-and-conditions) on Wiley Online Library for rules of use; OA articles are governed by the applicable Creative Commons License

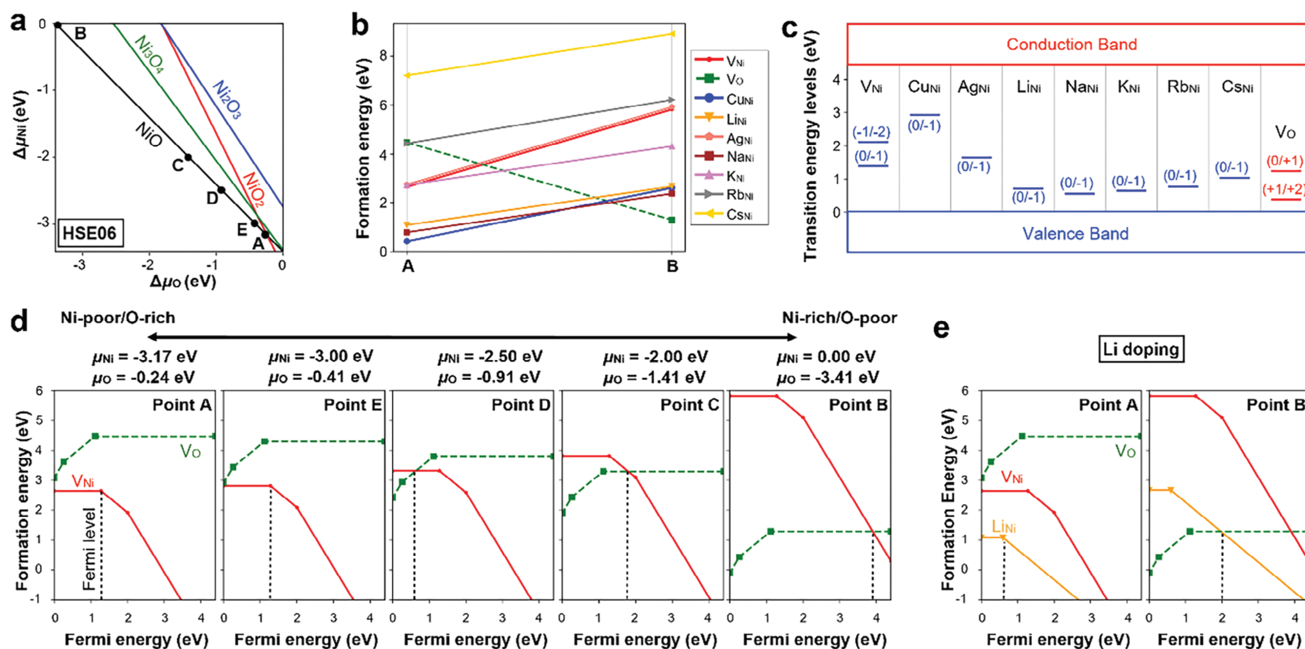

Figure 2. DFT calculation of intrinsic and extrinsic defects in NiO_x. a) Ni chemical potential $\Delta\mu_{Ni}$ as a function of the O chemical potential $\Delta\mu_O$. b) HSE06 calculated formation energies of intrinsic and extrinsic defects in neutral charge states as a function of chemical potential. c) HSE06 calculated transition energy levels of acceptor-like (blue color) and donor-like (red color) defects in NiO_x. d) HSE06 calculated defect formation energies of intrinsic point defects, as a function of the Fermi level at points A, B, C, D, and E, separately. e) HSE06 calculated defect formation energies of Li dopant as a function of the Fermi level at point A and point B, separately.

increasing the Li concentration, the defect formation energy of Li_{Ni} decreases and the corresponding pinned Fermi level is first set by Vo and Li_{Ni}, and then by the transition level of Li_{Ni} (0/-1).

Our DFT calculations show that the hole conductivity of NiO_x can be increased with acceptor density through the tuning of intrinsic defects with O-rich conditions and the generation of extrinsic acceptor-like defects through Li doping. To test this experimentally, we developed a sol-gel method to create NiO_x thin films with varied Li doping ratios. We used ultraviolet photoelectron spectroscopy (UPS) to obtain the work function (WF) and VBM, and optical absorption spectroscopy to obtain the bandgap (**Figure 3a**; Figure S6, Supporting Information). The energy difference between the WF and VBM decreases while the bandgap of NiO_x remains unchanged with Li doping, indicating an increased acceptor density. Using the experimentally found WF and VBM for the doped and undoped NiO_x, optoelectronic simulations show that an eight-fold increase of the hole injection into the QD layer can be expected (Figure S7, Supporting Information). The presence of Li in the NiO_x films was seen through a Li signal and peak shift of the O signal (Figure S8, Supporting Information) in the X-ray photoelectron spectroscopy (XPS) measurements.[13]

We fabricated metal–insulator–metal (MIM) devices to demonstrate the impact of Li doping on the conductivity of the NiO_x (Figure S9, Supporting Information).[14] We found that the conductivity increases with dopant concentration, and the highest conductivity is achieved with a Li concentration of 10% in the sol-gel precursor solution (Figure 3b). This is consistent

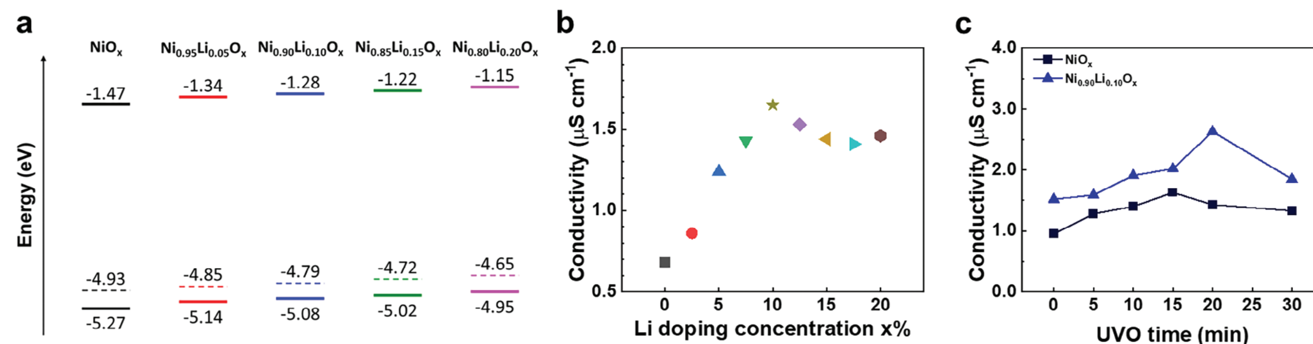

Figure 3. Experimental verification of intrinsic and extrinsic defects in NiO_x. a) Energy level diagram of NiO_x at varying Li doping concentrations. Conductivity of NiO_x and Li-doped NiO_x at varying b) Li doping concentrations and c) UVO time.

© 2024 Wiley-VCH GmbH

16136829, 0, Downloaded from https://onlinelibrary.wiley.com/doi/10.1002/smll.202402371 by University Of Toronto Librarie, Wiley Online Library on [11/04/2024]. See the Terms and Conditions (https://onlinelibrary.wiley.com/terms-and-conditions) on Wiley Online Library for rules of use; OA articles are governed by the applicable Creative Commons License

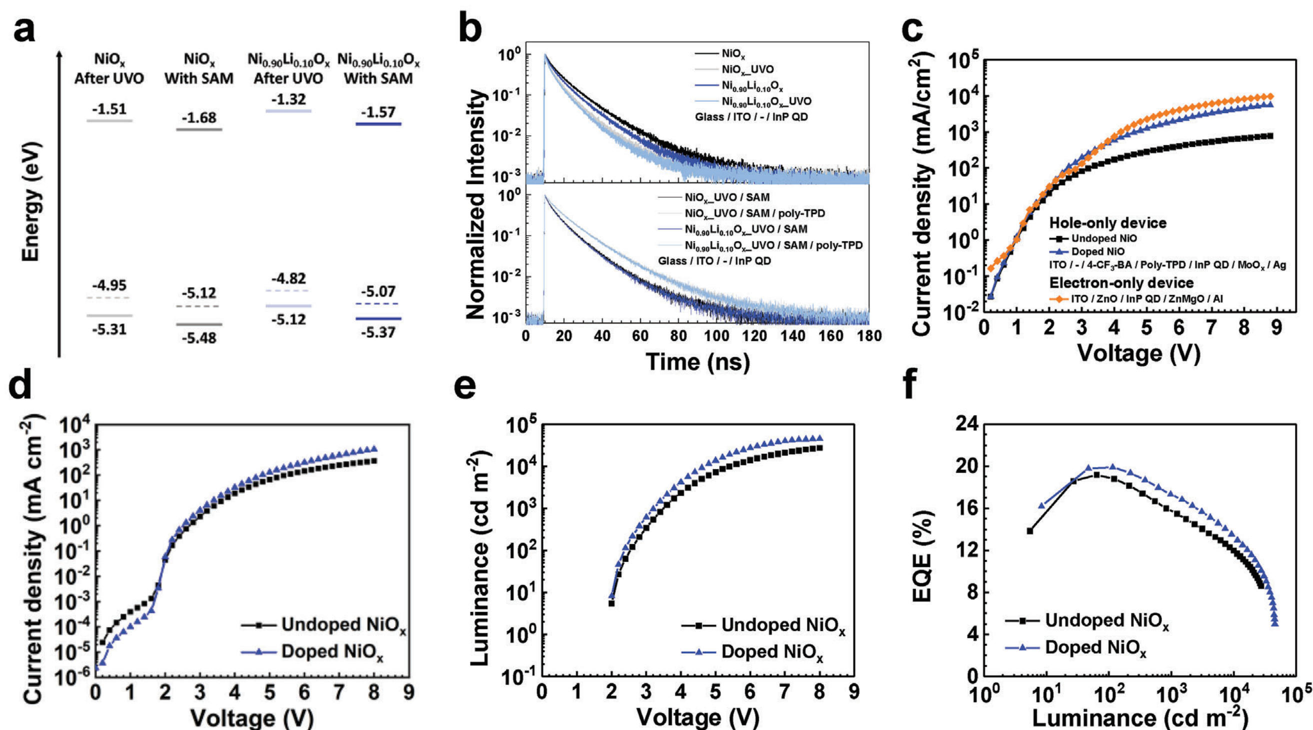

Figure 4. Performance of InP QLEDs based on optimized NiO_x HILs. a) Energy level diagram of NiO_x after UVO and Li-doped NiO_x after UVO with and without SAM, respectively. b) Time-resolved PL spectra of InP QD layers on undoped NiO_x and doped NiO_x. c) *J*–*V* characteristics of hole-only devices with undoped NiO_x and doped NiO_x and electron-only devices. d) *J*–*V* characteristics, e) *L*–*V* characteristics, f) EQE-*L* characteristics of InP QLEDs with undoped NiO_x and doped NiO_x as an HIL.

with DFT results that as Li concentration increases, the hole concentration increases first and then declines. Therefore, the conductivity, determined in part by hole concentration, exhibits the same trend.

Besides using Li doping for extrinsic defects, we also tuned intrinsic defects in NiO_x by creating an oxygen-rich stoichiometry, achieved through ultraviolet ozone (UVO) treatment, as shown in Figure 3c.[15] Using the same MIM architecture used in the Li-doping experiments (Figure S9, Supporting Information), we found that the conductivity of NiO_x films can be increased with the UVO treatment, without noticeable changes to film morphology (Figure S10, Supporting Information).

Our optoelectronic simulations showed that with an increase in the VBM, a barrier for hole injection is formed. The experimental results (Figure 3a) showed that Li doping concentration increases the VBM. On the other hand, the UVO treatment of NiO_x creates hydroxyl groups on the surface which decreases the VBM[10b] from −5.08 to −5.12 eV (**Figure 4**a; Figure S11, Supporting Information). To further tune the VBM, a SAM of 4-trifluoromethyl benzoic acid[6] was employed to shift the VBM to -5.37 eV for efficient hole injection into the poly-TPD (Figure 4a).

We further investigate the effect of Li doping and UVO treatment on the PL properties of the InP QD layer using time-resolved PL and PLQE measurements (Figure 4b; Tables S3 and S4, Supporting Information). One might posit that Li doping and UVO treatment could introduce exciton quenching sites[10b]; however, we find that in QLEDs, Li doping improves device performance without adversely affecting emission by the InP QDs. We offer that the SAM layer passivates NiO_x surface traps, and poly-TPD functions as a barrier separating the active layer from the trap states in the HIL. It will be of interest to explore further strategies to enhance hole injection in NiO_x without introducing exciton quenching sites, something that could potentially increase QLED performance without relying on SAMs and poly-TPD.

Balanced charge injection is necessary to realize efficient QLEDs. To assess the charge injection of holes and electrons, we conducted a comparison using half-cell devices consisting of hole-only devices (HODs) and electron-only devices (EODs) (Figure 4c). We found that the electron is the majority charge carrier, as evidenced by the higher current density in EODs compared to HODs. Importantly, the hole injection is significantly improved in the HOD with Li doping in the NiO_x HIL, which should lead to an improved balance of charge carrier injection in the InP QD layer in the QLEDs. We further estimated the trap density and carrier mobility[16] from the *J*–*V* characteristics of HODs and EODs (Figure S12, Supporting Information). The results indicated that the trap density remained substantially unchanged, whereas the mobility of NiO_x increased ≈4–5x following Li doping into NiO_x.

In light of increased hole injection seen in HOD at a Li concentration of 10%, we fabricated devices using doped NiO_x having a 10% concentration of Li. Irrespective of doping, the electroluminescence (EL) spectra show no difference in peak wavelength and full width at half maximum (FWHM) over a wide range of luminance *(L)* from 50 to 5000 cd m^{-2}. This confirms that

 © 2024 Wiley-VCH GmbH

16136829, 0, Downloaded from https://onlinelibrary.wiley.com/doi/10.1002/smll.202402371 by University Of Toronto Librarie, Wiley Online Library on [11/04/2024]. See the Terms and Conditions (https://onlinelibrary.wiley.com/terms-and-conditions) on Wiley Online Library for rules of use; OA articles are governed by the applicable Creative Commons License

defects in our NiO_x HIL do not affect the optical properties of the InP QD. Over this wide range of L, there is no emission from the poly-TPD HTL (Figure S13, Supporting Information), owing to the high hole injection efficiency and balanced charge injection in InP QD. The InP QLED with doped NiO_x exhibits increased current injection due to the improved hole injection as shown in Figure 4d. Moreover, the L_{Max} increases from 27 300 to 45 200 cd m^{-2}, and the EQE increases from 19.2% to 19.9%, as shown in Figure 4e,f, respectively. To our knowledge, this is a record amongst QLEDs with inorganic HILs (Table S5, Supporting Information). We also note that the operating stability of QLEDs is improved with the aid of doping of NiO_x (Figure S14, Supporting Information). These improvements are a result of the enhanced hole injection and balanced charge injection in the InP QD layer. We confirmed the improvements are reproducible based on a set of 20 samples (Figure S15, Supporting Information). Statistically, the L_{Max} and EQE of InP QLEDs are improved by 27% and 8%, respectively, with the use of our doped NiO_x HIL. Additionally, the turn-on voltage ($V_{Turn\text{-}on}$) is decreased from 2.1 to 2.0 V on average with doped NiO_x HIL, further confirming the improved hole injection. We note the need to work further on InP synthesis and surface management in order to minimize EQE roll-off. The SAM layer and UVO treatments increase current injection, contribute to increased L_{Max}, and improve efficiency in devices that employ doped NiO_x (Figure S16, Supporting Information).

3. Conclusion

To summarize, we developed an inorganic NiO_x-based HIL for QLEDs that contributes to increased LED efficiency. Optoelectronic simulations (SCAPS) reveal that changing the electronic properties of NiO_x, including lowering its VBM and increasing its acceptor density, is projected to improve hole injection efficiencies into the InP QD layer. DFT results show that increased acceptor density and correspondingly better hole injection can be achieved by controlling the intrinsic and extrinsic defects of NiO_x with UVO treatment and Li doping. With this guidance from the simulation, we then applied the combination of Li-doping and UVO strategies to enhance hole injection efficiency by increasing the acceptor density. We further used SAMs to tune the VBM to the desired band alignment for efficient hole injection into the InP QDs. These strategies lead to an EQE of 19.9%, a record amongst QLEDs with inorganic HILs.

4. Experimental Section

Materials: Nickel nitrate hexahydrate (Sigma-Aldrich, 99.999%), Lithium nitrate (Sigma-Aldrich, 99.99%), Ethylene glycol (Sigma-Aldrich, anhydrous, 99.8%), ethylenediamine (Sigma-Aldrich, ≥99%), poly-TPD (American Dye Sources Inc., ADS254BE), ZnO nanoparticle dispersions (Avantama N-10, 2.5 wt.%, 2-propanol) were used without purification.

SCAPS: To simplify the simulation and focus on the NiO_x HIL, a 1D model of the InP QLED with a planar InP layer was adopted using the SCAPS-1D (version 3.3.07), developed by the research team at the University of Gent lead by Marc Burgelman.[9b] To obtain a more focused understanding of the hole injection properties of NiO_x HILs, the detailed electronic properties with shell and 0-D geometries of QDs have been neglected. The simulation parameters are provided in Figure S7 (Supporting Information).

DFT Calculation: All calculations were performed using the FHI-aims[17] all-electron code. The default numerical settings, referred to as "tight" in FHI-aims were used. The basis sets used for all elements are given in Table S1 (Supporting Information). Spin-polarized treatment for the Ni atom was included in all calculations. More specifically, the NiO in all structures (unit cell and supercell) adopted a type-II anti-ferromagnetic phase (AF_2 spin arrangement, i.e., the spin ordering vectors are along [111] directions, the corresponding primitive-cell crystal structures are shown in Figure S1a, Supporting Information). The defect formation energies were calculated by the supercell approach based on a $3 \times 2 \times 3$ supercell (building based on the primitive shown in Figure S1a, Supporting Information, a total of 72 atoms). The local minimum-energy geometries of the Born-Oppenheimer surface for all the defect structures were obtained with residual total energy gradients below 1×10^{-2} eV Å^{-1} for atomic positions by PBE-GGA[18] functional within a Γ-centered k-grid $3 \times 3 \times 3$. The corresponding total energies and electronic properties for all the defects were calculated by short-range screened hybrid exchange-correlation functional HSE06[19] with a fixed screening parameter ($\omega = 0.2$ Å^{-1}) and exchange mixing parameter ($\alpha = 0.25$) based on a Γ-centered k-grid $3 \times 3 \times 3$.

In the supercell approach, the defect formation energy for a defect type, α in charge state q can be calculated according to the following equation[20]:

$$\Delta H\ (\alpha, q) = E\,(\alpha, q) - E\,(host) + \sum_i n_i\,(E_i + \Delta\mu_i) + q\,(\varepsilon_{VBM}\,(host) + E_F) + E_{corr}\,[\alpha, q] \quad (1)$$

Here, the $E(\alpha,q)$ and E(host) represent the total energy for the defects and host. The $\Delta\mu_i$ means the delta chemical potential of element i, which is based on the total energy E_i in the elemental solid phase. (More details can be found in the Note S1, Supporting Information) The E_F means the Fermi level, which is based on the VBM of the host. The E_{corr} is the correction term for the charge defects according to the Freysoldt–Neugebauer–Van de Walle (FNV) approximations.[21] The associated terms in the FNV approximations are obtained by using the Python script[41] within FHI-aims electrostatic potentials. (shown in Figures S3–S5, Supporting Information for all the considered defects) Based on these calculated charged defect formation energies, the transition states $E(\alpha, q^1/q^2)$ for specific defect type α can be further obtained based on the following equation:

$$\Delta H\ (\alpha, q^1) = \Delta H\,(\alpha, q^2) \quad (2)$$

$$E\ (\alpha,\ q^1/q^2) = \left(\left(E\,(\alpha,\ q^2) + E_{corr}\,[\alpha, q^2]\right) - \left(E\,(\alpha,\ q^1) + E_{corr}\,[\alpha, q^1]\right)\right) / \,(q^1 - q^2) \quad (3)$$

Characterization: UPS, XPS measurement was performed at nanoFAB, University of Alberta. UPS measurement was carried out using a Kratos Axis Ultra spectrometer was used for with a He I source ($h\nu = 21.2$ eV). The sample was measured under −10 V bias. The power for UPS was 3 kV × 20 mA (60 W). X-ray photoelectron measurement was carried out using a Thermo Scientific K-Alpha XPS system with an Ar ion gun. Optical absorption measurements were carried out in a Lambda 950 UV–vis–IR spectrophotometer. Time-resolved PL was measured using a Horiba Fluorolog system. A pulsed laser diode and a time-correlated single-photon counting (TCSPC) detector were used for time-resolved PL. The excitation wavelength was 504 nm for and time-resolved PL measurement.

Sol-Gel Processed NiO_x and Li-Doped NiO_x Film Fabrication: For the NiO_x and Li-doped NiO_x sol-gel solution, nickel nitrate hexahydrate and lithium nitrate were dissolved in ethylene glycol at a total concentration of 0.3 M with the desired atomic ratio for Li doping. Ethylenediamine was added as a stabilizer 1:1 molar ratio of metal ions to ethylenediamine molecules. The fully dissolved NiO_x and Li-doped NiO_x precursor solutions were filtered through a 0.45 µm polyvinylidene difluoride (PVDF) membrane before use and spin-coated at 3000 rpm for 30 s and annealed at 300 °C for 1 h. NiO_x and Li-doped NiO_x films were treated with UVO.

Device Fabrication and Measurement: The patterned ITO glass substrates (TFD Inc., 15 Ω sq^{-1}) were cleaned by sequential sonication in deionized water, acetone, and isopropyl alcohol. After drying in the oven,

© 2024 Wiley-VCH GmbH

16136829, 0, Downloaded from https://onlinelibrary.wiley.com/doi/10.1002/smll.202402371 by University Of Toronto Libraries, Wiley Online Library on [11/04/2024]. See the Terms and Conditions (https://onlinelibrary.wiley.com/terms-and-conditions) on Wiley Online Library for rules of use; OA articles are governed by the applicable Creative Commons License

the substrates were exposed to UVO treatment for 20 min. The NiO_x HIL was fabricated using the sol-gel process as described above. SAMs of the 4-(trifluoromethyl)benzoic acid were treated on the NiO_x HIL by spin-coating an anhydrous ethanol solution (2.5 mg mL^{-1}) at 5000 rpm for 20 s and annealed at 100 °C for 5 min. Unreacted SAM molecules were removed by washing with pure anhydrous ethanol via spin coating at 5000 rpm for 20 s and annealed again at 100 °C for 5 min. All substrates were transferred to an N_2-filled glovebox. Then, 150 µL of poly-TPD in chlorobenzene solution (8 mg mL^{-1}) was filtered through a 0.22 µm polytetrafluoroethylene (PTFE) membrane before use and spin-coated at 3000 rpm for 30 s and annealed at 140 °C for 10 min. The InP QD solution prepared according to a previously reported method,[4c] was filtered through a 0.22 µm PTFE membrane before use, and then spin-coated at 3000 rpm for 30 s, followed by annealing at 140 °C for 10 min. The ZnMgO nanoparticle dispersions, synthesized as described in the literature,[22] were filtered through a 0.22 µm PTFE membrane before use. The dispersions (30 mg mL^{-1} in anhydrous ethanol) were then spin-coated at 3000 rpm for 30 s, followed by annealing at 140 °C for 10 min. After ZnMgO nanoparticle coating, all substrates were transferred to a thermal evaporator (Angstrom Engineering), and a patterned Al electrode (100 nm thick) was deposited with a deposition rate of 1.0 Å s^{-1} under a vacuum pressure less than 2×10^{-6} torr.

MIM devices fabricated with the structure of Glass / ITO / HIL / MoO_x / Ag. For Ag and MoO_x, 100 nm Ag and 10 nm thick MoO_x were deposited with a rate of 1.0 and 0.1 Å s^{-1} under a vacuum pressure less than 2×10^{-6} Torr. Half-cell devices of HOD and EOD were fabricated with the structure of Glass / ITO / HIL / SAM / poly-TPD / InP QD / MoO_x / Ag and Glass / ITO / ZnO / InP QD / ZnMgO / Al, respectively. For the ZnO, ZnO nanoparticle dispersion was filtered through a 0.22 µm PTFE membrane before use, spin-coated at 3000 rpm for 30 s, and annealed at 140 °C for 10 min.

The J–V characteristics of devices were recorded using a Keithley 2400 source meter. EL spectra and L at a certain J–V point were measured using a calibrated fiber-coupled spectrometer (QE-pro, Ocean Optics) and an integrating sphere (FOIS-1, Ocean Optics). To ensure accurate measurements, the calibration of the equipment was performed using a radiometrically calibrated light source (HL-3P-INT-CAL, Ocean Optics). During the measurements, the QLED devices were positioned on top of the integration sphere to collect only the forward light emission, following the standard OLED characterization method.[23]

Supporting Information

Supporting Information is available from the Wiley Online Library or from the author.

Acknowledgements

H.W., E.D.J., T.Z., and S.M.P. contributed equally to this work. This work was supported by Samsung Electronics Co. (MRA211815). The authors thank D. Kopilovic, E. Palmiano, L. Levina, and R. Wolowiec for their technical support.

Conflict of Interest

The authors declare no conflict of interest.

Data Availability Statement

The data that support the findings of this study are available from the corresponding author upon reasonable request.

Keywords

charge transport layers, doping, light-emitting diodes, nickel oxide, quantum dots

Received: March 25, 2024
Published online:

[1] a) V. L. Colvin, M. C. Schlamp, A. P. Alivisatos, *Nature* **1994**, *370*, 354; b) Y. Shirasaki, G. J. Supran, M. G. Bawendi, V. Bulović, *Nat. Photonics* **2013**, *7*, 13; c) S. Coe, W.-K. Woo, M. Bawendi, V. Bulović, *Nature* **2002**, *420*, 800.
[2] a) J. H. Chang, D. Hahm, K. Char, W. K. Bae, *J. Inf. Disp.* **2017**, *18*, 57; b) D. V. Talapin, A. L. Rogach, A. Kornowski, M. Haase, H. Weller, *Nano Lett.* **2001**, *1*, 207; c) M. Danek, K. F. Jensen, C. B. Murray, M. G. Bawendi, *Chem. Mater.* **1996**, *8*, 173; d) D. V. Talapin, I. Mekis, S. Götzinger, A. Kornowski, O. Benson, H. Weller, *J. Phys. Chem. B* **2004**, *108*, 18826.
[3] a) A. A. Guzelian, J. E. B. Katari, A. V. Kadavanich, U. Banin, K. Hamad, E. Juban, A. P. Alivisatos, R. H. Wolters, C. C. Arnold, J. R. Heath, *J. Phys. Chem.* **1996**, *100*, 7212; b) Y. Li, X. Hou, X. Dai, Z. Yao, L. Lv, Y. Jin, X. Peng, *J. Am. Chem. Soc.* **2019**, *141*, 6448; c) O. I. Mićić, H. M. Cheong, H. Fu, A. Zunger, J. R. Sprague, A. Mascarenhas, A. J. Nozik, *J. Phys. Chem. B* **1997**, *101*, 4904.
[4] a) X. Dai, Z. Zhang, Y. Jin, Y. Niu, H. Cao, X. Liang, L. Chen, J. Wang, X. Peng, *Nature* **2014**, *515*, 96; b) H. Shen, Q. Gao, Y. Zhang, Y. Lin, Q. Lin, Z. Li, L. Chen, Z. Zeng, X. Li, Y. Jia, S. Wang, Z. Du, L. S. Li, Z. Zhang, *Nat. Photonics* **2019**, *13*, 192; c) Y.-H. Won, O. Cho, T. Kim, D.-Y. Chung, T. Kim, H. Chung, H. Jang, J. Lee, D. Kim, E. Jang, *Nature* **2019**, *575*, 634; d) C. Xiang, L. Wu, Z. Lu, M. Li, Y. Wen, Y. Yang, W. Liu, T. Zhang, W. Cao, S.-W. Tsang, B. Shan, X. Yan, L. Qian, *Nat. Commun.* **2020**, *11*, 1646.
[5] a) Y. Meng, Z. Hu, N. Ai, Z. Jiang, J. Wang, J. Peng, Y. Cao, *ACS Appl. Mater. Interfaces* **2014**, *6*, 5122; b) J.-M. Yun, J.-S. Yeo, J. Kim, H.-G. Jeong, D.-Y. Kim, Y.-J. Noh, S.-S. Kim, B.-C. Ku, S.-I. Na, *Adv. Mater.* **2011**, *23*, 4923.
[6] S. Lee, S. M. Park, E. D. Jung, T. Zhu, J. M. Pina, H. Anwar, F.-Y. Wu, G.-L. Chen, Y. Dong, T. Cui, M. Wei, K. Bertens, Y.-K. Wang, B. Chen, T. Filleter, S.-F. Hung, Y.-H. Won, K. H. Kim, S. Hoogland, E. H. Sargent, *J. Am. Chem. Soc.* **2022**, *144*, 20923.
[7] a) W. Cao, C. Xiang, Y. Yang, Q. Chen, L. Chen, X. Yan, L. Qian, *Nat. Commun.* **2018**, *9*, 2608; b) S. Chen, W. Cao, T. Liu, S.-W. Tsang, Y. Yang, X. Yan, L. Qian, *Nat. Commun.* **2019**, *10*, 765; c) T. Kim, K.-H. Kim, S. Kim, S.-M. Choi, H. Jang, H.-K. Seo, H. Lee, D.-Y. Chung, E. Jang, *Nature* **2020**, *586*, 385; d) J. H. Chang, P. Park, H. Jung, B. G. Jeong, D. Hahm, G. Nagamine, J. Ko, J. Cho, L. A. Padilha, D. C. Lee, C. Lee, K. Char, W. K. Bae, *ACS Nano* **2018**, *12*, 10231; e) X. Chen, X. Lin, L. Zhou, X. Sun, R. Li, M. Chen, Y. Yang, W. Hou, L. Wu, W. Cao, X. Zhang, X. Yan, S. Chen, *Nat. Commun.* **2023**, *14*, 284; f) J. Kwak, W. K. Bae, D. Lee, I. Park, J. Lim, M. Park, H. Cho, H. Woo, D. Y. Yoon, K. Char, S. Lee, C. Lee, *Nano Lett.* **2012**, *12*, 2362; g) F. So, D. Kondakov, *Adv. Mater.* **2010**, *22*, 3762.
[8] Y. Sun, W. Chen, Y. Wu, Z. He, S. Zhang, S. Chen, *Nanoscale* **2019**, *11*, 1021.
[9] a) Z. Yang, J. Z. Fan, A. H. Proppe, F. P. G. d. Arquer, D. Rossouw, O. Voznyy, X. Lan, M. Liu, G. Walters, R. Quintero-Bermudez, B. Sun, S. Hoogland, G. A. Botton, S. O. Kelley, E. H. Sargent, *Nat. Commun.* **2017**, *8*, 1325; b) M. Burgelman, P. Nollet, S. Degrave, *Thin Solid Films* **2000**, *361–362*, 527.
[10] a) S. Rhee, D. Hahm, H.-J. Seok, J. H. Chang, D. Jung, M. Park, E. Hwang, D. C. Lee, Y.-S. Park, H.-K. Kim, W. K. Bae, *ACS Nano* **2021**, *15*, 20332; b) F. Wang, Z. Wang, X. Zhu, Y. Bai, Y. Yang, S. Hu, Y. Liu, B. You, J. Wang, Y. Li, Z. a. Tan, *Small* **2021**, *17*, 2007363; c) J. Deng, M. Mortazavi, N. V. Medhekar, J. Z Liu, *J. Appl. Phys.* **2012**, *112*, 123703.
[11] a) D. Di Girolamo, F. Di Giacomo, F. Matteocci, A. G. Marrani, D. Dini, A. Abate, *Chem. Sci.* **2020**, *11*, 7746; b) U. S. Joshi, Y.

© 2024 Wiley-VCH GmbH

16136829, 0, Downloaded from https://onlinelibrary.wiley.com/doi/10.1002/smll.202402371 by University Of Toronto Librarie, Wiley Online Library on [11/04/2024]. See the Terms and Conditions (https://onlinelibrary.wiley.com/terms-and-conditions) on Wiley Online Library for rules of use; OA articles are governed by the applicable Creative Commons License

Matsumoto, K. Itaka, M. Sumiya, H. Koinuma, *Appl. Surf. Sci.* **2006**, *252*, 2524.
[12] Z. Qiu, H. Gong, G. Zheng, S. Yuan, H. Zhang, X. Zhu, H. Zhou, B. Cao, *J. Mater. Chem. C* **2017**, *5*, 7084.
[13] a) X. Xia, Y. Jiang, Q. Wan, X. Wang, L. Wang, F. Li, *ACS Appl. Mater. Interfaces* **2018**, *10*, 44501; b) J. Y. Zhang, W. W. Li, R. L. Z. Hoye, J. L. MacManus-Driscoll, M. Budde, O. Bierwagen, L. Wang, Y. Du, M. J. Wahila, L. F. J. Piper, T. L. Lee, H. J. Edwards, V. R. Dhanak, K. H. L. Zhang, *J. Mater. Chem. C* **2018**, *6*, 2275.
[14] W. Chen, Y. Wu, Y. Yue, J. Liu, W. Zhang, X. Yang, H. Chen, E. Bi, I. Ashraful, M. Grätzel, L. Han, *Science* **2015**, *350*, 944.
[15] a) A. Klasen, P. Baumli, Q. Sheng, E. Johannes, S. A. Bretschneider, I. M. Hermes, V. W. Bergmann, C. Gort, A. Axt, S. A. L. Weber, H. Kim, H.-J. Butt, W. Tremel, R. Berger, *J. Phys. Chem. C* **2019**, *123*, 13458; b) J. Kim, Y. S. Kim, H. R. Jung, W. Jo, *Appl. Surf. Sci.* **2021**, *555*, 149625; c) T.-Y. Lin, T. T. Pfeiffer, P. B. Lillehoj, *RSC Adv.* **2017**, *7*, 37374.
[16] W. Shen, Y. Yu, W. Zhang, Y. Chen, J. Zhang, L. Yang, J. Feng, G. Cheng, L. Liu, S. Chen, *ACS Appl. Mater. Interfaces* **2022**, *14*, 5682.
[17] a) V. Blum, R. Gehrke, F. Hanke, P. Havu, V. Havu, X. Ren, K. Reuter, M. Scheffler, *Comput. Phys. Commun.* **2009**, *180*, 2175; b) V. Havu, V. Blum, P. Havu, M. Scheffler, *J Comput Phys* **2009**, *228*, 8367; c) X. Ren, P. Rinke, V. Blum, J. Wieferink, A. Tkatchenko, A. Sanfilippo, K. Reuter, M. Scheffler, *New J Phys* **2012**, *14*, 053020.
[18] J. P. Perdew, K. Burke, M. Ernzerhof, *Phys. Rev. Lett.* **1996**, *77*, 3865.
[19] J. Heyd, G. E. Scuseria, M. Ernzerhof, *J. Chem. Phys.* **2003**, *118*, 8207.
[20] S. Lany, A. Zunger, *Phys. Rev. B* **2008**, *78*, 235104.
[21] a) Y. Kumagai, F. Oba, *Phys. Rev. B* **2014**, *89*, 195205; b) C. Freysoldt, J. Neugebauer, C. G. Van de Walle, *Phys. Rev. Lett.* **2009**, *102*, 016402.
[22] H. Moon, W. Lee, J. Kim, D. Lee, S. Cha, S. Shin, H. Chae, *Chem. Commun.* **2019**, *55*, 13299.
[23] S.-H. Jeong, J. Park, T.-H. Han, F. Zhang, K. Zhu, J. S. Kim, M.-H. Park, M. O. Reese, S. Yoo, T.-W. Lee, *Joule* **2020**, *4*, 1206.

 © 2024 Wiley-VCH GmbH

16136829, 0, Downloaded from https://onlinelibrary.wiley.com/doi/10.1002/smll.202402371 by University Of Toronto Librarie, Wiley Online Library on [11/04/2024]. See the Terms and Conditions (https://onlinelibrary.wiley.com/terms-and-conditions) on Wiley Online Library for rules of use; OA articles are governed by the applicable Creative Commons License